Effects of maturation on the conformational free-energy landscape of SOD1

Robert M. Culik[a,b,c,1], Ashok Sekhar[a,b,c,1,2], Jayashree Nagesh[d], Harmeen Deol[e], Jessica A. O. Rumfeldt[e], Elizabeth M. Meiering[e], and Lewis E. Kay[a,b,c,f,2]

[a]Department of Molecular Genetics, University of Toronto, Toronto, ON M5S 1A8, Canada; [b]Department of Biochemistry, University of Toronto, Toronto, ON M5S 1A8, Canada; [c]Department of Chemistry, University of Toronto, Toronto, ON M5S 1A8, Canada; [d]Chemical Physics Theory Group, Department of Chemistry, University of Toronto, Toronto, ON M5S 3H6, Canada; [e]Department of Chemistry, University of Waterloo, Waterloo, ON N2L 3G1, Canada; and [f]Program in Molecular Medicine, Hospital for Sick Children, Toronto, ON M5G 1X8, Canada

Edited by G. Marius Clore, National Institutes of Health, National Institute of Diabetes and Digestive and Kidney Diseases, Bethesda, MD, and approved January 31, 2018 (received for review December 3, 2017)

Amyotrophic lateral sclerosis (ALS) is a devastating fatal syndrome characterized by very rapid degeneration of motor neurons. A leading hypothesis is that ALS is caused by toxic protein misfolding and aggregation, as also occurs in many other neurodegenerative disorders, such as prion, Alzheimer's, Parkinson's, and Huntington's diseases. A prominent cause of familial ALS is mutations in the protein superoxide dismutase (SOD1), which promote the formation of misfolded SOD1 conformers that are prone to aberrant interactions both with each other and with other cellular components. We have shown previously that immature SOD1, lacking bound Cu and Zn metal ions and the intrasubunit disulfide bond (apoSOD1^{2SH}), has a rugged free-energy surface (FES) and exchanges with four other conformations (excited states) that have millisecond lifetimes and sparse populations on the order of a few percent. Here, we examine further states of SOD1 along its maturation pathway, as well as those off-pathway resulting from metal loss that have been observed in proteinaceous inclusions. Metallation and disulfide bond formation lead to structural transformations including local ordering of the electrostatic loop and native dimerization that are observed in rare conformers of apoSOD1^{2SH}; thus, SOD1 maturation may occur via a population-switch mechanism whereby posttranslational modifications select for preexisting structures on the FES. Metallation and oxidation of SOD1 stabilize the native, mature conformation and decrease the number of detected excited conformational states, suggesting that it is the immature forms of the protein that contribute to misfolded conformations in vivo rather than the highly stable enzymatically active dimer.

SOD1 | NMR | excited conformational states | CPMG | CEST

Cu,Zn-superoxide dismutase (SOD1) is a homo-dimeric metalloenzyme that acts to decrease oxidative stress in cells (1). In its fully mature state, each SOD1 subunit binds a copper ion and a zinc ion, and is stabilized further by an intramolecular disulfide connecting Cys-57 and Cys-146 (Cu,Zn-SOD1$^{S\text{-}S}$) (1). The *sod1* gene was the first to be linked to the familial form of amyotrophic lateral sclerosis (fALS) (2), with >150 identified mutations accounting for ∼20% of the inherited disease, while 90% of ALS is sporadic. Aggregated SOD1 is observed in inclusion bodies from ALS patients (3) as well as from mouse models of this fatal neurodegenerative disease (4). Symptoms of neurodegeneration in mice appear earlier than aggregates can be detected in the spinal cord (5), suggesting that smaller misfolded forms of SOD1 initiate disease. Fully mature Cu,Zn-SOD1$^{S\text{-}S}$ is remarkably stable (6), with a melting temperature of 92 °C, and, as such, an unlikely candidate for a protein conformational disorder. Instead, it has been proposed that immature forms of SOD1, which are significantly less stable, are the origin for cytotoxic misfolded conformations (7, 8).

The maturation pathway of SOD1 is illustrated in Fig. 1*A*. In the first step, apoSOD1^{2SH}, which lacks metal ions and disulfides and is predominantly monomeric in solution (9, 10), acquires zinc by a process that is yet unknown. The E,Zn-SOD1^{2SH} maturation state was reported to be largely dimeric based on gel filtration assays performed by Furukawa and O'Halloran (11), although subsequent mass spectrometric studies provided evidence that this species is predominantly monomeric (12). Subsequent metalation of E,Zn-SOD1^{2SH} to Cu,Zn-SOD1^{2SH} (12) followed by oxidation to Cu,Zn-SOD1$^{S\text{-}S}$ (12) is facilitated by a copper chaperone, CCS (13, 14), a three domain-containing protein where domains 1 and 3 are involved in copper transport/delivery and disulfide bond formation, while domain 2 is highly homologous to SOD1 with ∼50% sequence identity. A crystal structure of the yeast SOD1–CCS heterodimer reveals that the SOD1–CCS interaction occurs through the SOD1 canonical homodimer interface (15). This implies that at least some fraction of E,Zn-SOD1^{2SH} exists as a monomer, as was also observed by Furukawa and coworkers using size exclusion chromatography (SEC).

Although the states described above and illustrated in Fig. 1 (on pathway) are thought to be the only ones populated along the maturation pathway of SOD1, previous studies have shown that other maturation states can exist in vivo and in disease-related aggregates. For example, Rotilio and coworkers (16) have shown that the metal-free, disulfide-oxidized form of SOD1 (apoSOD1$^{S\text{-}S}$) is present in diseased rat livers. Another example is provided by the study of Borchelt and coworkers (17), where a mutant of SOD1 lacking the copper-binding site was found to be highly aggregation prone and neurotoxic. In addition, studies in

Significance

Copper, zinc superoxide dismutase 1 (SOD1) is an enzyme involved in free radical scavenging in the cell. Despite the high stability of the mature protein, mutations, covalent modifications, and increased populations of immature forms result in instability and misfolding of SOD1 that is neurotoxic. Here, we study how the structure and dynamics of SOD1 change as a function of maturation. We find that as SOD1 progresses to its final active conformation, the free-energy landscapes for each successive state along the maturation pathway appear to become smoother with less exploration of higher energy conformations. Our results suggest that maturation may occur via a series of steps in which the transiently populated structures of preceding states successively become the dominant conformations.

Author contributions: R.M.C., A.S., E.M.M., and L.E.K. designed research; R.M.C., A.S., and H.D. performed research; J.N. and J.A.O.R. contributed new reagents/analytic tools; R.M.C., A.S., J.N., H.D., E.M.M., and L.E.K. analyzed data; and R.M.C., A.S., E.M.M., and L.E.K. wrote the paper.

The authors declare no conflict of interest.

This article is a PNAS Direct Submission.

[1]R.M.C. and A.S. contributed equally to this work.

[2]To whom correspondence may be addressed. Email: ashok.sekhar@utoronto.ca or kay@pound.med.utoronto.ca.

This article contains supporting information online at www.pnas.org/lookup/suppl/doi:10.1073/pnas.1721022115/-/DCSupplemental.

Published online February 26, 2018.

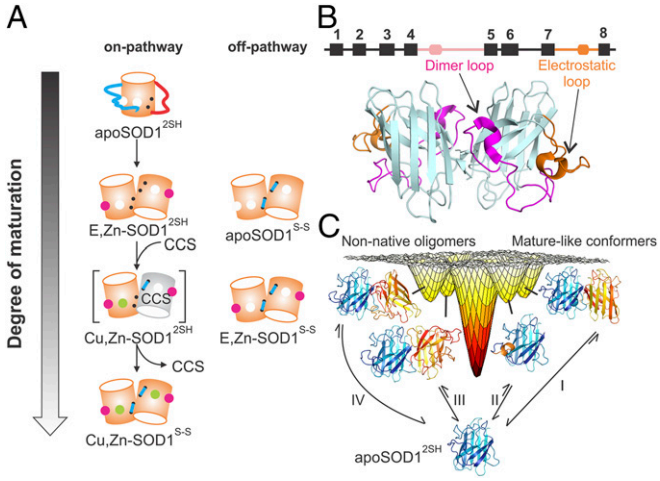

Fig. 1. The SOD1 maturation pathway. (*A*) Schematic representation of the SOD1 maturation pathway. Off-pathway maturation states relevant to this study are also shown. Zinc and copper metals are depicted as magenta and green spheres, respectively; the electrostatic (dimer) loop is shown as a long cyan (red) line; and the intrasubunit disulfide is depicted with a short cyan line connecting two black dots, representing the two Cys residues in each pWT SOD1 monomer. The dimer and electrostatic loops are shown in a squiggly manner because they are disordered in apoSOD1^{2SH}. The gray cylinder is a CCS monomer. (*B*) Cartoon representation of the 3D structure of dimeric Cu,Zn-SOD1^{S-S} (Protein Data Bank ID code 1HL5; ref. 26), with the dimer and electrostatic loops colored in magenta and orange, respectively. A schematic of the secondary structure is shown above the cartoon with the eight β-strands depicted as black rectangles; the dimer and electrostatic loops in pink and orange, respectively; and the short helices in the "loop regions" as rounded rectangles. (*C*) The previously determined rugged free-energy landscape of immature apoSOD1^{2SH} (10), showing exchange processes that lead to as many as four different excited states in equilibrium with native apoSOD1^{2SH}. Two of these excited states (*Right*), formed as a result of processes I and II, have structural features similar to those for mature Cu,Zn-SOD1^{S-S}. The excited-state structure formed via process I closely resembles the native dimer, while the rare state in process II contains a locally folded electrostatic loop, as in the mature dimer. The other two conformers (*Left*, generated via processes III and IV) are nonnative oligomers whose formation highlights the propensity of apoSOD1^{2SH} to form aberrant interactions.

K562 human cells have established that a fraction of SOD1 in cells exists in a copper-free state (18).

It is clear that there are a number of on- and off-pathway conformers that can ultimately lead to the formation of mature SOD1 (summarized in Fig. 1*A*) or potentially to aberrant forms of the molecule that might be implicated in disease. It is of interest, therefore, to characterize both the structural properties of each of these states and their dynamics, focusing on excited state conformers (i.e., conformers that are higher in energy than the ground state) that are thermally accessible from each state to gain insight into their respective free-energy surfaces (FESs). Solution NMR spectroscopy is a particularly powerful technique for studies of transiently formed sparsely populated states of biomolecules, even in cases where these states cannot be observed directly using traditional biophysical methods (19, 20). It is worth noting that such studies of rare protein conformations can be telling. In a recent study of disease mutants of SOD1, we observed little change to the structures of the ground state in each case relative to the WT protein while there were significant changes to the numbers and types of rare conformers for each mutant (21).

Here, we present a solution NMR dynamics study focusing on picosecond–nanosecond and microsecond–millisecond motional timescales to probe the FESs of SOD1 on- and off-pathway maturation states using both WT and the A4V disease mutant proteins. Notably, early on-pathway conformers are found to exchange with rare states that structurally resemble the next stage in maturation, thereby opening up kinetic pathways for maturation. Maturation of SOD1 proceeds with restriction of conformational space, such that no thermally accessible excited conformations could be detected for the fully mature, enzymatically active state, Cu,Zn-SOD1^{S-S}. Our results provide support for the hypothesis that immature intermediates of SOD1 are an important source of cytotoxic conformations in ALS pathology.

Results

NMR Experiments Provide Insight into the FES of apoSOD1^{2SH}. We have shown previously that pseudo-WT (pWT) apoSOD1^{2SH}, in which surface-exposed Cys-6 and Cys-111 are replaced by Ala and Ser, respectively (10), retains the eight-stranded β-barrel structure of Cu,Zn-SOD1^{S-S} (Fig. 1*B*; pWT is implicitly assumed throughout and only added when needed for clarity). However, apoSOD1^{2SH} is far more dynamic on the picosecond–nanosecond timescale than the mature protein (10). This is particularly the case for the extensive dimer and electrostatic loops that become well-structured in the mature state but that are clearly disordered in the immature form of the enzyme. In addition to the increased picosecond–nanosecond motion, apoSOD1^{2SH} is highly dynamic on the millisecond timescale and transiently samples four excited states that are shown in Fig. 1*C* (10). These four rare conformers are either on- or off-pathway from the perspective of SOD1 maturation. For example, one of the exchange processes (termed process I) involves the interconversion between monomeric apoSOD1^{2SH} and a native-like dimer conformation, while a second process converts a loop in apoSOD1^{2SH} to a helix that is found in the fully mature Cu,Zn-SOD1^{S-S} structure (process II). Another pair of conformers are formed via processes that are off-pathway (III and IV), involving aberrant intermolecular interactions.

Characterization of the FES of apoSOD1^{2SH} (10) has been possible largely by applying a pair of powerful experiments that probe conformational exchange processes between populated ground state conformers and less populated excited conformational states. Because these experiments also form the basis for characterizing the FESs of states that are both on and off the maturation pathway in what follows, we briefly review the basic features of each. In the first experiment, called chemical exchange saturation transfer (CEST) (20, 22), a very weak radiofrequency (B_1) field, typically between 5 and 50 Hz, is applied for a specific duration across frequencies covering the chemical shift range (one at a time) for the nucleus type in question and the intensity of the visible ground state peak is monitored as a function of the B_1 field position. When the field is applied at frequencies distal from the resonance positions of the spin of interest in either the ground or excited states, there is no change to the intensity of the ground state peak, I. In contrast, when the position of the B_1 field coincides with frequency of the invisible excited state peak, the subsequent perturbation to it is transferred to the ground state resonance via chemical exchange, resulting in an attenuated signal. When the field is applied on-resonance to the ground state peak I decreases to zero due to saturation. Thus, for a two-site chemical exchange process, a plot of I as a function of the position of the B_1 field consists of major and minor dips at the resonance positions of the spin in the ground and excited states, respectively. In a second experiment, called Carr–Purcell–Meiboom–Gill (CPMG) relaxation dispersion (23, 24), the effective transverse relaxation rate, $R_{2,\text{eff}}$, of an exchanging spin is quantified as a function of the number of chemical shift refocusing pulses that are applied in an interval of fixed duration. A plot of $R_{2,\text{eff}}$ vs. ν_{CPMG} [$= 1/(2\delta)$, where δ is the time between pules] produces a CPMG dispersion profile where nonflat curves are the hallmark of chemical exchange. In what follows, we will study both the on- and off-pathway maturation states of SOD1 using CEST and CPMG experiments to obtain insight into how their FESs evolve during the maturation process.

It is worth emphasizing that the CEST and CPMG relaxation approaches, described above, are restricted in terms of the timescales of exchange events that can be quantified, so that only certain regions of a given FES can be explored. Notably, CEST and CPMG methods are sensitive to exchange rates between ~50–500 and 100–3,000 s^{-1}, respectively, and to populations of rare states on the order of 0.5% or higher (corresponding to a free-energy difference between the ground and excited states <3 kcal/mol) (19). The degree of ruggedness of a given FES, as we define it, and hence the number of different conformers that can be observed is, of course, an NMR-based measure, subject to the limitations mentioned above.

Zinc Titration of apoSOD1^{2SH}. The first step toward maturation of SOD1 is the formation of E,Zn-SOD1^{2SH} by the binding of Zn to apoSOD1^{2SH}. We followed this process by carrying out a Zn titration in which increasing concentrations of zinc chloride were added to a 1.2 mM sample of apoSOD1^{2SH}. During the course of the titration, some of the peaks decreased in intensity while others appeared as a function of added Zn. The pattern of peak changes was consistent with slow exchange between Zn-free and Zn-bound states. Note that while there is only one Zn ion per SOD1 monomer in the enzymatically active form of the protein, Zn can also bind to the copper site (25) in the presence of superstoichiometric amounts of metal. During the course of the titration, the intensities of the original peaks from apoSOD1^{2SH} were quantified, as were a series of new peaks that appeared and on the basis of the intensity profiles the peaks were grouped into four separate classes, as exemplified in Fig. 2 *A*–*D*. These include the following: (*i*) peaks from apoSOD1^{2SH} that decrease in intensity during the course of the titration (Fig. 2*A*), (*ii*) peaks from E,Zn-SOD1^{2SH} that increase in intensity until a 1:1 $[Zn]_{Tot}/[SOD1]_{Tot}$ ratio is reached and then decrease subsequently as the Zn,Zn-SOD1^{2SH} state is formed (Fig. 2*B*), (*iii*) peaks that have degenerate chemical shifts for E,Zn-SOD1^{2SH} and Zn,Zn-SOD1^{2SH} and consequently increase until a 1:1 ratio of metal to protein is achieved and then plateau (Fig. 2*C*), and (*iv*) peaks from Zn,Zn-SOD1^{2SH} for which intensity is obtained only after a 1:1 ratio (Fig. 2*D*). To verify that peaks from E,Zn-SOD1^{2SH} are the result of Zn binding to the Zn site of SOD1, we acquired a ^{1}H–^{15}N heteronuclear multiple-bond correlation spectroscopy (HMBC) spectrum of E,Zn-SOD1^{2SH} focusing on the His side chains. The positions of peaks from His-63, 71, and 80, which are the ligating residues for the Zn ion (26), are identical to the corresponding peaks in a spectrum of Cu,Zn-SOD1$^{S\text{-}S}$, confirming that SOD1 is metallated in the manner expected (Fig. S1).

The steep increases in the intensities of peaks from E,Zn-SOD1^{2SH} until a $[Zn]_{Tot}/[SOD1]_{Tot}$ ratio of 1:1 is achieved followed by a decrease in intensities, as well as the lack of any intensity for the peaks reporting on the Zn,Zn-SOD1^{2SH} state until a 1:1 ratio is surpassed clearly indicates that binding is sequential with the first Zn-binding site saturating before the second binding event occurs. Accordingly, a total of 35 titration profiles from peaks belonging to all four classes described above were globally fit to the sequential binding model shown at the *Top* of Fig. 2*E* using equations in *Supporting Information* to extract K_{d1} and K_{d2} values of 27 ± 25 nM and 80 ± 20 μM, respectively (25 °C). The model visually fits the data well, and 1D reduced χ^2 surfaces as a function of K_{d1} and K_{d2} (Fig. 2*E*) establish that, while K_{d2} (~100 μM) can be obtained reliably, the surface for K_{d1} is flat below values of ~0.1 μM; 0.1 μM is, therefore, an upper bound for the dissociation of Zn from the Zn-binding site, a result that is consistent with the value of 75 ± 25 nM for K_{d1} obtained previously using chemical denaturation (27). Our results confirm that Zn binding to the Cu site is at least two orders of magnitude weaker than the interaction with the Zn site, providing a post facto justification for the sequential model used in fitting the data.

Structure and Dynamics of the Electrostatic Loop in E,Zn-SOD1^{2SH}. The ^{1}H–^{15}N heteronuclear single-quantum coherence spectroscopy (HSQC) spectrum of E,Zn-SOD1^{2SH} is significantly different from that of apoSOD1^{2SH} (Fig. S2), with a number of new peaks appearing at ^{1}H chemical shifts between 9.5–11 and 6–7.5 ppm, where very few backbone amides of apoSOD1^{2SH} resonate. These peaks can be assigned to residues in the electrostatic loop (122–140, Fig. 1*B*), suggesting that major structural changes occur in this region upon Zn binding. To understand how the electrostatic loop reorganizes in response to binding zinc, we compared ^{15}N and ^{1}H chemical shifts of this region from spectra of E,Zn-SOD1^{2SH} and apoSOD1^{2SH} (Fig. 3 *A* and *B*), since chemical shifts are sensitive reporters of protein structure. As expected, there is little correlation in chemical shifts, indicating that the loop structure has significantly changed from the disordered conformation that is found in apoSOD1^{2SH} (10). In contrast, backbone ^{1}H and ^{15}N chemical shifts of the electrostatic loop residues in E,Zn-SOD1^{2SH} correlate very well with the shifts of the corresponding residues in Cu,Zn-SOD1$^{S\text{-}S}$ (Fig. 3*C*), unequivocally demonstrating that the electrostatic loop has attained its fully mature structure in E,Zn-SOD1^{2SH}.

The significant structural changes to the ground state that accompany Zn binding prompted us to explore whether there are corresponding changes to the electrostatic loop region in any rare conformers that might potentially be visited by E,Zn-SOD1^{2SH}. As described above and in previous papers (10, 21), disordered residues 131–138 in apoSOD1^{2SH} that are part of the electrostatic loop form a helix in an excited state (process II, Fig. 1*C*), a secondary structural element that is present in the ground state of the fully mature form of the enzyme. Evidence for the excited state can be seen in the CEST traces of residues Asn-131 and Thr-135 of apoSOD1^{2SH} (green) with the small dips in each case positioned at the amide ^{15}N resonance frequencies for these residues in the helical conformation (Fig. 3*D*) (10). Notably, the CEST profiles for Asn-131/Thr-135 of apoSOD1^{2SH}, E,Zn-SOD1^{2SH}, and Cu,Zn-SOD1$^{S\text{-}S}$ clearly establish that this excited state of apoSOD1^{2SH} matches well with the ground states of E,Zn-SOD1^{2SH} and Cu,Zn-SOD1$^{S\text{-}S}$, implying that E,Zn-SOD1^{2SH} also has a locally folded helix in the electrostatic loop. The dipole of this helix faces the Zn binding site (28), suggesting that the presence of Zn in its canonical position in the protein stabilizes this helix and hence the excited state conformation (process II) of apoSOD1^{2SH}. Notably, CEST traces for Asn-131/Thr-135 of both E,Zn-SOD1^{2SH} and Cu,Zn-SOD1$^{S\text{-}S}$ show only a single (major) dip, suggesting that excited conformers with significant structural changes in this region are not present in either of these two states.

Having established that the electrostatic loop is stabilized in the ground state of E,Zn-SOD1^{2SH} to a conformation resembling that in the mature enzyme, we next investigated whether the significant amplitude fast (picosecond–nanosecond) timescale dynamics of this region in the apoSOD1^{2SH} state ($^{15}N\{^{1}H\}$ NOE values of 0.2–0.4, Fig. 3*E*, *Left*) are reduced upon metallation. That this is the case is evident from the increased $^{15}N\{^{1}H\}$ NOE values for E,Zn-SOD1^{2SH} (0.6–0.8, Fig. 3*E*, *Middle*) that more closely resemble those measured in Cu,Zn-SOD1$^{S\text{-}S}$ (Fig. 3*E*, *Right*). Taken together, these results show that the binding of Zn to its canonical site leads to a structured and rigid electrostatic loop with a conformation similar to that found in the mature, enzymatically active form of SOD1.

Thermodynamic, Kinetic, and Structural Characterization of the E,Zn-SOD1^{2SH} Oligomerization State. Having established that the electrostatic loop becomes structured upon Zn binding to apoSOD1^{2SH}, we next sought to establish how other structural properties, such as oligomerization, are affected by metallation. Fig. 4*A* shows measured backbone ^{15}N transverse relaxation rates (R_2) for monomeric apoSOD1^{2SH}, E,Zn-SOD1^{2SH}, and dimeric Cu,Zn-SOD1$^{S\text{-}S}$. In the

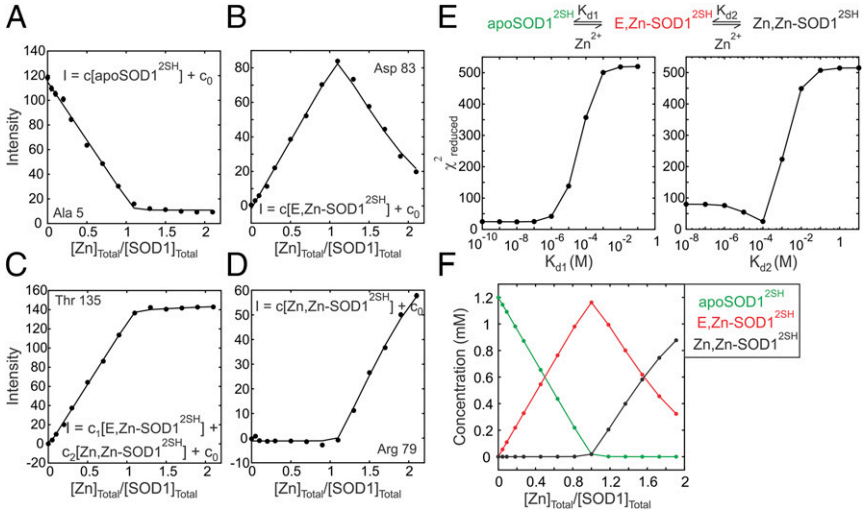

Fig. 2. NMR-detected binding of Zn^{2+} to apoSOD1^{2SH}. (*A–D*) Binding curves showing intensities of cross-peaks in ^{1}H–^{15}N HSQC spectra as a function of the ratio of the total Zn^{2+} and SOD1^{2SH} (i.e., total monomer) concentrations. Zn^{2+} can bind either to the Zn or the Cu site in an apoSOD1^{2SH} monomer, and each panel (*A–D*) presents a representative example of the four classes of peaks that report on the binding events. Intensity profiles in *A*, *B*, and *D* are associated with peaks reporting on the concentrations of apoSOD1^{2SH}, E,Zn-SOD1^{2SH}, and Zn,Zn-SOD1^{2SH} states, respectively, while in *C* a representative profile for a peak with degenerate chemical shifts for singly and doubly Zn-bound states is shown. Errors in peak intensities are generally smaller than the size of the data points. Solid lines are global fits of the data to the sequential binding model shown in *E*. For each class, intensities were related to the concentrations of the molecular species present during the titration as indicated on the plots, where c_0 is a peak-specific constant that relates to the noise floor of the spectrum. (*E*) Reduced χ^2 surfaces for dissociation equilibrium constants K_{d1} (binding to the Zn site) and K_{d2} (binding to the Cu site) showing that while K_{d2} (=80 ± 20 μM) can be determined from the fit, only an upper bound for K_{d1} (0.1 μM) can be obtained. (*F*) Variation in the populations of apoSOD1^{2SH}, E,Zn-SOD1^{2SH}, and Zn,Zn-SOD1^{2SH} during the titration obtained from a simulation using the model in *E* and the best-fit values of equilibrium constants K_{d1} and K_{d2}.

macromolecular limit, R_2 rates are proportional to the overall tumbling time that, in turn, scales with molecular weight for a spherical particle. Notably, R_2 values for E,Zn-SOD1^{2SH} are larger than for apoSOD1^{2SH} but smaller than for Cu,Zn-SOD1$^{S\text{-}S}$, suggesting that E,Zn-SOD1^{2SH} may exist as a monomer–dimer mixture at the concentrations where the experiment was performed (1 mM in total monomer concentration, 25 °C). Using the average R_2 values for apoSOD1^{2SH} and Cu,Zn-SOD1$^{S\text{-}S}$ as proxies for monomer and dimer transverse relaxation rate constants, respectively, we estimate a 16% fractional population for the monomer in a 1 mM solution of E,Zn-SOD1^{2SH} (i.e., $[M]/([M] + 2[M_2]) = 0.16$, where $[M]$ and $[M_2]$ are the concentrations of the monomers and dimers, respectively). Note that this estimation assumes that the exchange between monomer–dimer states is fast on the NMR chemical shift timescale and compared with differences in R_2 rates in the monomer and dimer structures.

To quantify the monomer–dimer equilibrium further, we conducted isothermal titration calorimetry (ITC) experiments. Small volumes of concentrated, predominantly dimeric, E,ZnSOD1^{2SH} solution were successively diluted into buffer, and the associated heats of dimer dissociation, which occurs due to mass action, were measured (Fig. S3). The ITC data are well fit by a two-state model, $2M \rightleftharpoons M_2$, providing an equilibrium dissociation constant, K_d, of 51 μM (25 °C), and the corresponding enthalpy of dissociation, ΔH_d, of 4.0 kcal·(mol monomer)$^{-1}$ (Fig. S3). Based on this K_d, a 1 mM solution of E,ZnSOD1^{2SH} will have a fractional monomer concentration of 15%, which is in agreement with the analysis of R_2 rates above. The K_d for E,ZnSOD1^{2SH} is 6,700- and 23,000-fold larger than for apoSOD1$^{S\text{-}S}$ and Cu,Zn SOD1$^{S\text{-}S}$, 7.6 and 2.2 nM, respectively (29, 30). In contrast, relative to apoSOD1^{2SH}, which has a K_d in the millimolar range (10), binding of Zn clearly substantially promotes dimerization. We also determined the value of ΔC_p for E,ZnSOD1^{2SH} dimer dissociation as 0.22 kcal·(mol monomer)$^{-1}$·°C^{-1} from the temperature dependence of ΔH_d (Fig. S3). This ΔC_p is much smaller than the value of 0.85 kcal·(mol monomer)$^{-1}$·°C^{-1} for apoSOD1$^{S\text{-}S}$ dimer dissociation (29), and 1.1 kcal·(mol monomer)$^{-1}$·°C^{-1} for global unfolding of apoSOD1^{2SH} (31), due to the highly dynamic nature of this immature protein. Together, the calorimetry data demonstrate that the dimer interface is much weaker and buries markedly less surface area in E,ZnSOD1^{2SH} than in more structured forms of SOD1 containing the intrasubunit disulfide bond.

The formation of a weak dimeric interface in E,Zn-SOD1^{2SH} is consistent with the absence of cross-peaks in ^{1}H–^{15}N HSQC spectra for the interfacial residues 49–54 of the dimer loop. Their absence cannot be explained by rapid hydrogen exchange with the solvent because residues from the electrostatic loop, which are more solvent-exposed than the dimer interface residues, can be visualized as strong peaks in the same dataset. To eliminate the possibility that these residues were overlapped in the crowded E,Zn-SOD1^{2SH} spectrum, we implemented amino acid-specific labeling to obtain a simplified spectrum. The dimer loop sequence (^{50}FGDNT^{54}) has three unique i, $i + 1$ residue pairs (FG, DN, and NT), which would allow for unambiguous detection via standard HNCO-based experiments (32) if the carbonyl carbon of residue i and the nitrogen of residue $i + 1$ are labeled with ^{13}C and ^{15}N, respectively, in a $^{12}C/^{14}N$ background. However, when this approach was used for both the FG and the DN pairs, one pair at a time, resonances were not visible in the HNCO dataset for F50(^{13}CO)-G51(^{15}N) or D52(^{13}CO)-N53(^{15}N). Finally, these residues could be clearly observed in spectra of dimeric apoSOD1$^{S\text{-}S}$ and Cu,Zn-SOD1$^{S\text{-}S}$, so their absence in datasets recorded of E,Zn-SOD1^{2SH} is not a reflection of the size of the system studied. Rather, our results provide evidence that residues 49–54 of the dimer loop interface are broadened beyond detection by microsecond–millisecond conformational exchange, reinforcing that the dimer interface is not stably formed in E,Zn-SOD1^{2SH}.

To characterize the kinetics of the oligomerization process and to gain insight into the structure at the dimer interface, we performed ^{15}N-CEST experiments on a 1 mM sample of E,Zn-SOD1^{2SH}. While residues 49–54 are not detected in spectra, G114, also at the dimer interface, can be quantified. We have previously shown that G114 is a good reporter of the apoSOD1^{2SH} monomer–dimer equilibrium, with a large ^{15}N shift change between the two

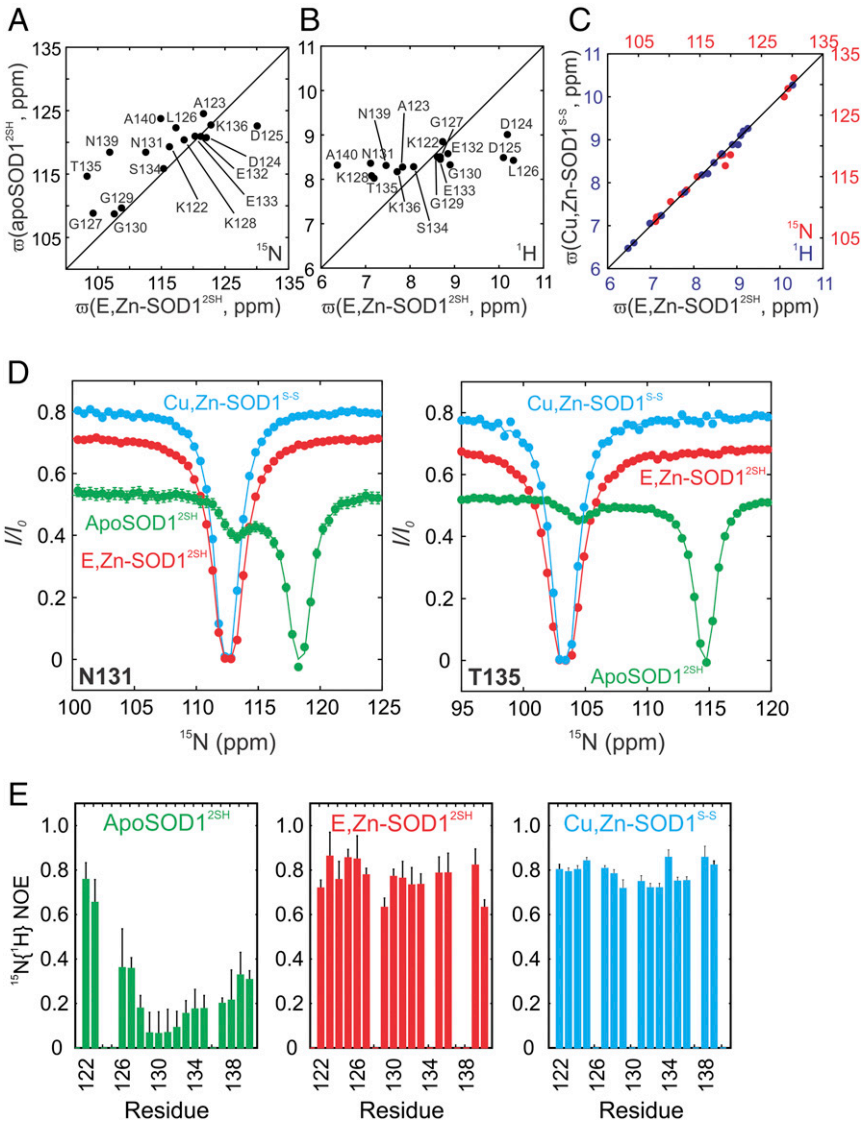

Fig. 3. The electrostatic loop in E,Zn-SOD1^{2SH} adopts a native-like configuration. Correlation plots of (*A*) ^{15}N chemical shift values for residues in the electrostatic loop of E,Zn-SOD1^{2SH} and apoSOD1^{2SH}. (*B*) ^{1}H chemical shifts for the same residues in E,Zn-SOD1^{2SH} and apoSOD1^{2SH} and (*C*) ^{1}H (blue) and ^{15}N (red) chemical shifts for the electrostatic loop residues in E,Zn-SOD1^{2SH} and Cu,Zn-SOD1^{S-S}. (*D*) ^{15}N-CEST profiles for Asn-131 (*Left*) and Thr-135 (*Right*) in the electrostatic loop of E,Zn-SOD1^{2SH} (red), compared with the most immature apoSOD1^{2SH} (green) and the enzymatically active Cu,Zn-SOD1^{S-S} (cyan) states. Single-residue fits of the data to a two-site model of chemical exchange, as described previously (10), are shown by solid lines. Differences in CEST baselines arise from different R_1 rates due to different tumbling times for apoSOD1^{2SH} (effectively all monomeric), E,Zn-SOD1^{2SH} (monomer–dimer equilibrium), and Cu,Zn-SOD1^{S-S} (all dimeric) states. (*E*) ^{15}N{^{1}H} NOE values for the electrostatic loop residues in the same maturation states as *D*.

interconverting states (10). The ^{15}N-CEST profiles of Gly-114 from E,Zn-SOD1^{2SH} (red) and apoSOD1^{2SH} (green) are shown in Fig. 4*B* where it is clear that for this residue the excited state of E,Zn-SOD1^{2SH} (small dip) has a similar backbone ^{15}N amide chemical shift as for G114 in the apoSOD1^{2SH} ground state and vice versa, suggesting that the monomer of E,Zn-SOD1^{2SH} has similar structural features as apoSOD1^{2SH} in the vicinity of G114. This profile is also consistent with a dominant dimeric conformation for E,Zn-SOD1^{2SH}. We then repeated the ^{15}N-CEST measurements on a sample of A4V E,Zn-SOD1^{2SH}, which was determined to be monomeric in solution based on R_2 data. The A4V mutation causes a particularly aggressive form of ALS and disrupts the dimer interface (1). As expected, the resonance position of the amide nitrogen for G114 in the ground state of A4V E,Zn-SOD1^{2SH} coincides with the G114 ^{15}N chemical shift in the excited state of pWT E,Zn-SOD1^{2SH} and vice versa (Fig. 4*C*). To further confirm that the exchange process observed for A4V E,Zn-SOD1^{2SH} corresponds to a monomer–dimer interconversion, and hence so too does the process characterized for pWT E,Zn-SOD1^{2SH}, an additional CEST experiment was recorded on the A4V sample at a twofold lower overall protein concentration (Fig. 4*D*). The CEST minor dip decreases markedly in size, establishing that the CEST profiles are reporting on a concentration-dependent event. Taken together, our results on A4V E,Zn-SOD1^{2SH} and pWT E,Zn-SOD1^{2SH} provide strong evidence of monomer–dimer exchange reactions, with the dominant conformation being a monomer for A4V and a dimer for pWT E,Zn-SOD1^{2SH}.

Although reliable exchange parameters for the $2M \underset{k_{off}}{\overset{k_{on}}{\rightleftarrows}} M_2$ reaction could not be obtained from a fit of only a single CEST profile in E,Zn-SOD1^{2SH} reporting on the monomer–dimer exchange reaction (G114), more accurate values could be obtained by fixing the populations of the interconverting states to those

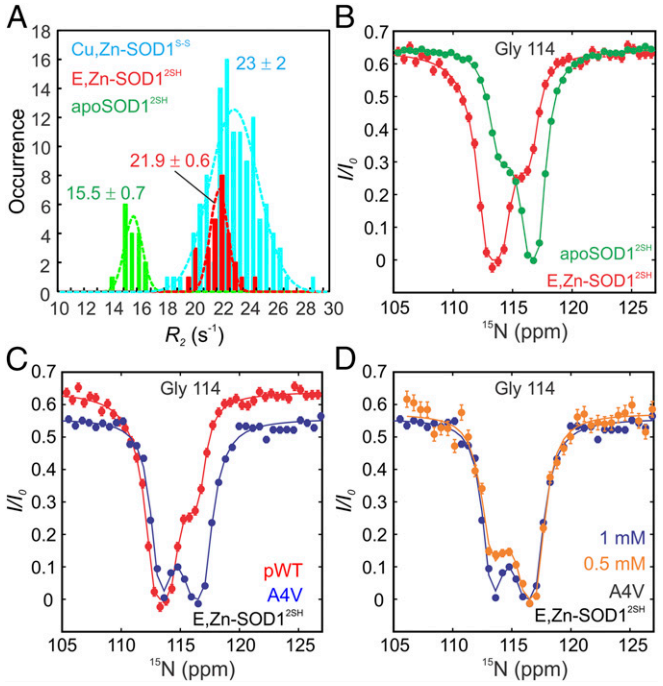

Fig. 4. E,Zn-SOD1^{2SH} is predominantly dimeric, but populates a small amount of monomer at equilibrium. (*A*) Distributions of R_2 values for SOD1 maturation states, as indicated. Dashed lines are fits of the distributions to a Gaussian function, with a mean and SD as indicated. (*B*) ^{15}N-CEST profiles for G114 of pWT apoSOD1^{2SH} (green) and E,Zn-SOD1^{2SH} (red) reporting on native dimerization (process I in Fig. 1*C*). While apoSOD1^{2SH} is predominately monomeric and exchanges with a native-like dimer, E,Zn-SOD1^{2SH} is predominantly dimeric in equilibrium with a small population of monomer. (*C*) ^{15}N-CEST profiles of Gly-114 in the E,Zn-SOD1^{2SH} state for pWT (red) and A4V (blue) SOD1. The A4V mutation disrupts the native dimer interface of SOD1, so that A4V E,Zn-SOD1^{2SH} exchanges between monomer (major) and dimer (minor) conformations with the reverse for pWT E,ZnSOD1^{2SH}. (*D*) ^{15}N-CEST profiles of A4V Gly-114 in the E,Zn-SOD1^{2SH} maturation state as a function of concentration. The decrease in the size of the minor dip at the lower protein concentration (orange) confirms that the exchange event involves a process that is dependent on protein concentration. Solid lines in *B*–*D* are fits of the data to a two-state model of conformational exchange.

predicted using K_d = 51 μM determined from ITC. In this way, values of k_{on} and k_{off} of (2.3 ± 0.4)10^4 M^{-1}·s^{-1} and 1.2 ± 0.2 s^{-1}, respectively, were fit. Notably, a small population of monomeric E,Zn-SOD1^{2SH} positions the protein for the next stage in the maturation pathway involving interaction with CCS for Cu transfer and establishment of the intrasubunit disulfide link.

Changes in E,Zn-SOD1^{2SH} upon Addition of CCS. The interaction of E,Zn-SOD1^{2SH} with CCS promotes the final stage of SOD1 maturation whereby Cu is transferred from the chaperone to the SOD1 Cu-binding site and the disulfide bond is formed. The CCS–SOD1 interaction has been studied in the literature by trapping E,Zn-SOD1^{2SH} as a heterodimeric complex with CCS in the absence of Cu (33). Here, we added Cu-loaded CCS to a solution of E,Zn-SOD1^{2SH} and acquired an NMR spectrum after several minutes of incubation. The ^{1}H–^{15}N HSQC spectrum (Fig. S4) of the resulting solution is virtually identical to that of Cu,Zn-SOD1^{S-S}. To verify the oxidation states of the sulfhydryl groups in the NMR sample, we performed SEC where reduced and oxidized SOD1 elute differently. The size exclusion chromatograms confirm that addition of Cu-loaded CCS to E,Zn-SOD1^{2SH} indeed results in fully mature, enzymatically active Cu,Zn-SOD1^{S-S} (Fig. S5).

Characterizing the FESs of SOD1 On- and Off-Pathway Maturation States. To examine how the conformational preferences of different maturation states of SOD1 are affected by posttranslational modifications such as metallation and disulfide bond formation, we have carried out a combined CEST and CPMG study, focusing on cross-peaks that report on processes I–IV (Fig. 1*C*). As described above, several important insights could be obtained from studies of the initial on-pathway state, corresponding to the E,Zn-SOD1^{2SH} conformer. First, local folding of the electrostatic loop (process II) is complete. Unlike apoSOD1^{2SH}, which is predominantly monomeric, E,Zn-SOD1^{2SH} is shifted toward the dimeric form, which cannot interact with CCS because CCS competes with SOD1 for binding at the homodimer interface. However, E,Zn-SOD1^{2SH} interconverts between dimeric and monomeric states (Fig. 4*B*), reminiscent of process I for apoSOD1^{2SH}, and facilitating heterodimer formation with CCS. Notably, processes III and IV are quenched upon Zn binding to apoSOD1^{2SH} (Fig. S6). Because the heterodimeric CCS/SOD1 complex forms too transiently for studies via CEST and CPMG experiments, little information can be obtained on this complex. However, relaxation studies of the long-lived fully mature Cu,Zn-SOD1^{S-S} form of the enzyme establish that processes I–IV are all eliminated (Fig. 3*D* and Fig. S6), suggesting that the FES of this species is smoothened relative to the more rugged landscape of apoSOD1^{2SH}.

Having qualitatively characterized how the FESs of SOD1 evolve with maturation, we next focused on off-pathway species apoSOD1^{S-S} and E,Zn-SOD1^{S-S} (Fig. 1*A*). While these states are not directly populated during SOD1 maturation, they can be formed in vivo upon loss of metal from mature SOD1, especially in the case of metal-binding deficient ALS mutants such as G85R or H46R for which the affinities of SOD1 for Zn and Cu ions are lowered (34). Fig. 5 shows the results of CEST- and CPMG-based studies of apoSOD1^{S-S} and E,Zn-SOD1^{S-S}, focusing, as above, on processes I–IV (highlighted in the figure). For reference, we have included results for apoSOD1^{2SH} for which all interconversion processes are observed. Upon oxidation of Cys-57 and Cys-146 to form apoSOD1^{S-S}, processes I, III, and IV are eliminated. This is to be expected, as apoSOD1^{S-S} forms a stable dimer, with average ^{15}N R_2 relaxation rates that are similar to those obtained for the mature holo-form of the enzyme (27 ± 2 vs. 23 ± 2 s^{-1} for the apo and metallated states, respectively). Thus, monomer–dimer exchange is quenched because the equilibrium is highly skewed to the dimeric structure (process I) and the dimer interface is not available to form aberrant structures (processes III and IV). Notably, without Zn, the electrostatic loop remains dynamic and the coil-to-helix transition of process II is present. A similar scenario with respect to quenching of the oligomerization processes is observed for E,Zn-SOD1^{S-S}. In this case, however, Zn binding stabilizes the electrostatic loop helix and hence eliminates process II as well. Thus, Zn binding and cysteine-bridging rigidify opposite ends of the SOD1 molecule, with the dimer interface retaining flexibility in E,Zn-SOD1^{2SH}, while the mobility of the electrostatic loop persists in apoSOD1^{S-S}. Either of these two posttranslational modifications is sufficient to quench the aberrant nonnative oligomerization processes that are observed for the apoSOD1^{2SH} form.

Correlation Between Microsecond–Millisecond and Picosecond–Nanosecond Dynamics in SOD1. Fig. 6 shows residue-specific ^{15}N{^{1}H} NOE values for apoSOD1^{2SH}, apoSOD1^{S-S}, and Cu,Zn-SOD1^{S-S}. In the case of apoSOD1^{2SH}, very low values are obtained for residues in the dimer and electrostatic loops, indicating that these regions are mobile on the picosecond–nanosecond timescale (35). In apoSOD1^{S-S}, NOEs remain very low for backbone amides in the electrostatic loop. We have not been able to obtain complete assignments for residues in the dimer loop, as many of the expected peaks in this region are not present in spectra; however, the first 20 residues are assigned and the ^{15}N{^{1}H} NOEs derived from them

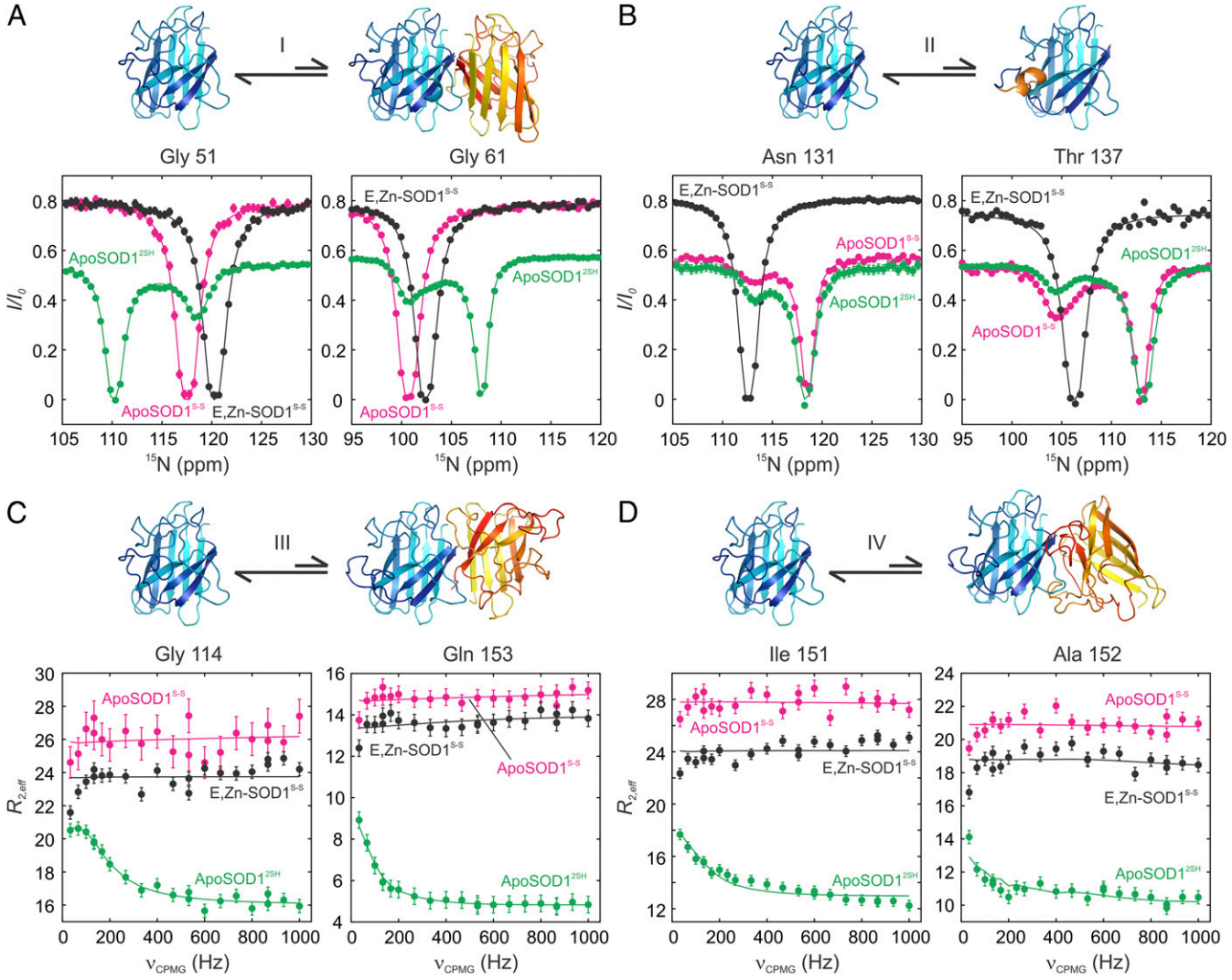

Fig. 5. Exploring the free-energy landscapes of apoSOD1$^{S\text{-}S}$ and E,Zn-SOD1$^{S\text{-}S}$ off-pathway states. ^{15}N-CEST (*A* and *B*) and ^{15}N-CPMG (*C* and *D*) profiles of the off-pathway maturation states apoSOD1$^{S\text{-}S}$ and E,Zn-SOD1$^{S\text{-}S}$, compared with immature apoSOD1^{2SH}, reporting on native dimerization (*A*, process I), formation of the electrostatic helix (*B*, process II), and nonnative oligomerization [symmetric dimer, process III (*C*), and asymmetric dimer, process IV (*D*)]. Single-residue fits of the CEST data to a two-state model of chemical exchange are shown. Differences in the baselines of CEST profiles reflect different R_1 relaxation rate constants that arise from different tumbling times between monomeric (apoSOD1^{2SH}) or dimeric (apoSOD1$^{S\text{-}S}$, E,Zn-SOD1$^{S\text{-}S}$) states or in the case of Asn-131 from the fact that this residue is part of a highly dynamic loop for both apo states that rigidifies upon the addition of metal. CPMG data from all residues associated with a given process are included in fits. Baselines of dispersion profiles for apoSOD1$^{S\text{-}S}$ and E,Zn-SOD1$^{S\text{-}S}$ are elevated relative to apoSOD1^{2SH} because of the faster transverse relaxation for the dimeric species.

are uniformly high. As expected, for the most part large NOEs are measured for Cu,Zn-SOD1$^{S\text{-}S}$ across its backbone. Interestingly, for both on- and off-pathway states, regions showing low NOE values and hence very rapid dynamics correspond to those for which slower millisecond timescale exchange processes and alternate sparely populated conformers are observed. For example, in the case of apoSOD1^{2SH}, residues 49–54 of the dimer loop for which low ^{15}N{^{1}H} NOE values are obtained, participate in the formation of a transient native-like dimer (process I). In a similar manner, a transient helix forms on the millisecond timescale in a region of the electrostatic loop that is highly mobile in the picosecond–nanosecond regime (process II). Upon cysteine oxidation to form apoSOD1$^{S\text{-}S}$ NOE values for the dimer loop increase and the corresponding slower process involving monomer–dimer exchange is no longer observed, while picosecond–nanosecond and millisecond dynamics persist in a region of the electrostatic loop that samples a helical structure in this state. Finally, the four millisecond exchange processes observed for apoSOD1^{2SH} are quenched in the Cu,Zn-SOD1$^{S\text{-}S}$ mature state of the enzyme with very significant attenuation of picosecond–nanosecond timescale motions as well. A correlation between picosecond–nanosecond backbone fluctuations and slower motions that are linked to catalytic function in enzymes has been described previously by Kern and coworkers (36). In the present case, the shift to a stable, well-defined conformation leads to quenching of motions over a range of timescales that is perhaps not surprising given that loops are involved in each process. Interestingly, while conformational diffusion in unstructured loops is typically fast (approximately nanosecond to microsecond) (37–39), the slower mobility observed for the exchange processes in SOD1 might originate from the additional topological constraints that these loops experience by virtue of the fact that they are tethered to an eight-stranded β-barrel core.

Discussion

NMR spin relaxation experiments offer unique opportunities to characterize the FESs of biologically important molecules in an

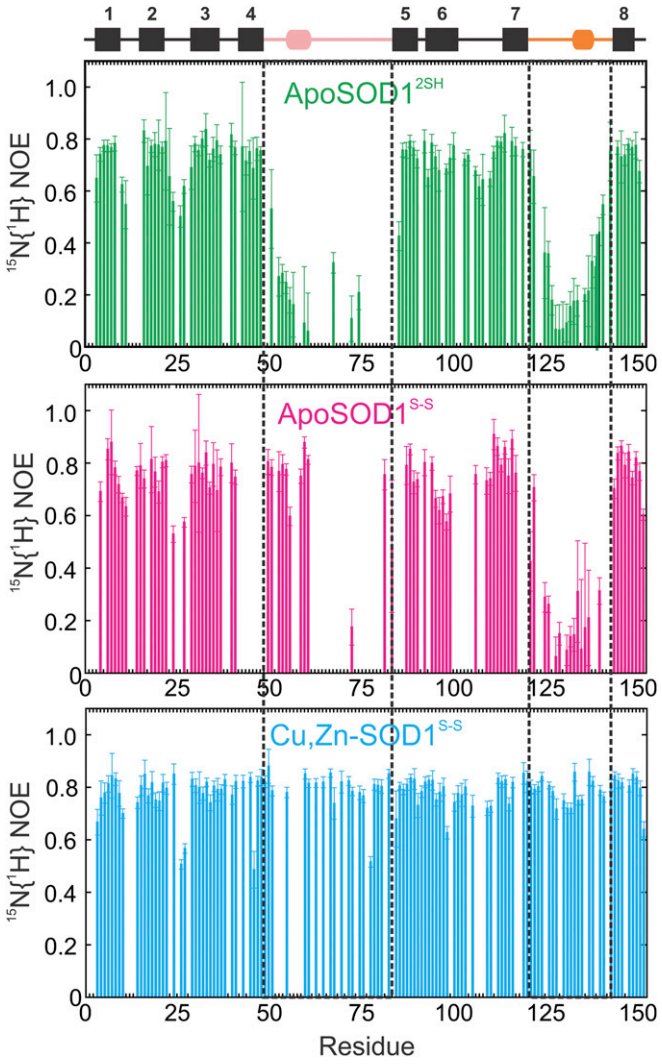

Fig. 6. Mobility of backbone amide bond vectors measured via $^{15}N\{^1H\}$ NOEs. Residue-specific $^{15}N\{^1H\}$ NOE values as proxies of local picosecond–nanosecond mobility for apoSOD1^{2SH} (*Top*), apoSOD1$^{S\text{-}S}$ (*Middle*), and Cu,Zn-SOD1$^{S\text{-}S}$ (*Bottom*). The protein secondary structure is indicated at the *Top* of the plot, as in Fig. 1*B*. Areas with significant local motions on the picosecond–nanosecond timescale (small NOE values) correlate with regions undergoing transient excursions to rare conformations (millisecond timescale), which include the dimer and electrostatic loops in apoSOD1^{2SH} and the electrostatic loop in apoSOD1$^{S\text{-}S}$. Cu,Zn-SOD1$^{S\text{-}S}$, with little fluctuation of backbone amides on the picosecond–nanosecond timescale, does not detectably populate any excited state.

effort to understand how the formation of rare conformational states might affect biological function (19, 20). Here, we have used a number of different NMR experiments to investigate the picosecond–nanosecond and millisecond timescale dynamics of SOD1 molecules along the maturation cycle of the enzyme. In the cell, SOD1 molecules undergo a series of maturation events after synthesis that increasingly stabilize them (14), leading finally to an enzymatically active form, as depicted in Figs. 1*A* and 7. Using a combination of CEST and CPMG NMR experiments, we previously demonstrated that the most immature state of SOD1, apoSOD1^{2SH}, which has been hypothesized to be the primary source of toxic misfolded conformations implicated in SOD1 ALS pathology (7, 8), interconverts between a populated ground state structure and various thermally accessible conformations (10). These include both native-like and aberrant structures (Fig. 1*C*). It has been unclear, however, how the SOD1 FES evolves as a function of maturation, both for on- and off-pathway conformers, and whether some of the same excited state structures are populated on the FESs of these states.

Our results suggest that the FESs of the different maturation states of SOD1 become progressively smoother as the extent of posttranslational modification increases (Fig. 7). For example, binding of one equivalent of Zn to apoSOD1^{2SH} (E,Zn-SOD1^{2SH}) rigidifies the electrostatic loop and shifts the monomer–dimer equilibrium observed in the apo state toward the dimeric form. However, the dimer is not stable, with a measured K_d of 51 μM at 25 °C, and so it may readily sample a monomer conformation under physiological conditions (~40 μM dimer in cells) (40). We hypothesize that transient sampling of the monomer may be essential for the interaction of SOD1 with its Cu chaperone CCS. From SEC-based binding experiments (Fig. S5), we and others have observed that apoSOD1^{2SH}, whose major state is monomeric, binds less tightly to CCS than E,Zn-SOD1^{2SH} even though it is more dimeric. This suggests that monomeric E,Zn-SOD1^{2SH} has a preorganized dimer interface that preferentially binds to CCS, in contrast to apoSOD1^{2SH}, which does not present a complementary interface. Further evidence to this effect comes from NMR data where residues in the dimer loop, including the critical region from Glu49-Thr54 that is at the holo dimer interface, are not visible in either ^1H- or ^{13}C-detected spectra. This region is broadened from conformational exchange that likely includes the sampling of structures with a preorganized dimer

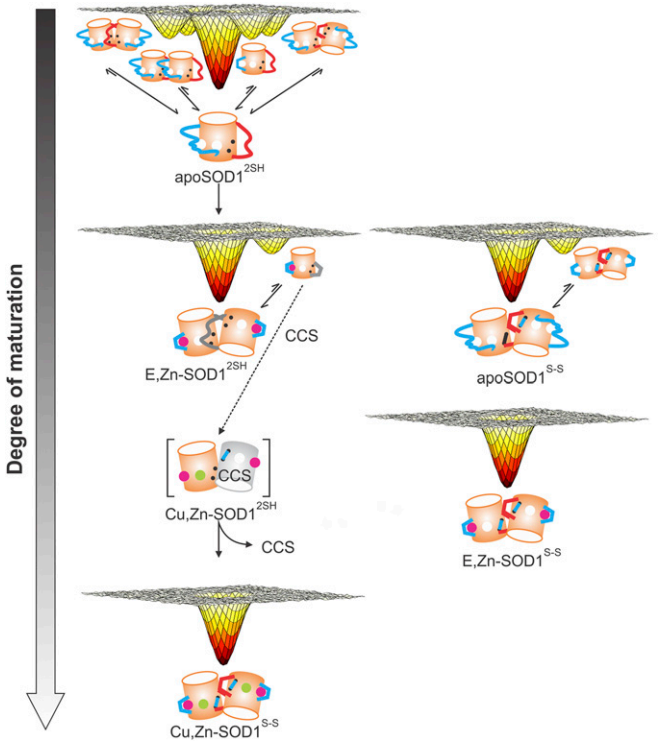

Fig. 7. Progressive smoothening of SOD1 free-energy landscapes as a function of maturation. Changes in the free-energy landscape of SOD1 upon maturation as observed using CEST and CPMG NMR experiments. Zinc and copper ions are depicted by magenta and green spheres, the electrostatic and dimer loops are represented by long cyan and red lines, and the intrasubunit disulfide as a short cyan line connecting two black dots. Squiggly dimer and electrostatic loops indicate that they are disordered, while loops denoted by straight lines indicate that they are rigid. The gray-colored dimer loop in E,Zn-SOD1^{2SH} signifies that there is no direct NMR information on this loop, although the available NMR data do strongly point to a conformationally dynamic region. The gray cylinder is a CCS monomer.

interface primed for CCS binding. Further evidence for the importance of a properly organized surface comes from the work of Banci et al. (12) showing that while apoSOD1^{2SH} is able to form heterodimers negligible copper transfer from CCS to SOD1 occurs, in contrast to E,Zn-SOD1^{2SH}. That E,Zn-SOD1^{2SH} is able to sample a monomeric state, likely with a complementary interface to CCS, potentially provides a facile route for SOD1 maturation (see below). Previous studies by Matthews and coworkers (41) also suggest that preorganization plays a role in E,Zn-SOD1$^{S\text{-}S}$ homodimerization.

The final step in the maturation process takes E,Zn-SOD1^{2SH} to Cu,Zn-SOD1$^{S\text{-}S}$ via the CCS chaperone, and NMR spin relaxation measurements indicate that the four excited states observed for apoSOD1^{2SH} are no longer transiently sampled (at least at detectable levels) in the FES of the mature form of the enzyme. The coil–helix exchange process (process II) is detected in the off-pathway apoSOD1$^{S\text{-}S}$ state, although the other processes are not, while none of the four processes can be observed in CEST/CPMG datasets recorded on the E,Zn-SOD1$^{S\text{-}S}$ state (Fig. 7).

Our studies of the FESs of intermediates along the SOD1 maturation pathway suggest that the maturation process may occur via a series of steps in which the transiently populated structure of an immediately preceding state may subsequently become the dominant conformer, as has been observed for the dihydrofolate reductase (DHFR) enzymatic cycle (42). Posttranslational modifications could thus induce structural transitions by simply selecting the appropriate conformation and executing a population switch by altering the relative stabilities of the ground and excited states. For example, one of the excited states of apoSOD1^{2SH} orders the electrostatic loop that then primes this region for Zn binding to form E,Zn-SOD1^{2SH} where the electrostatic loop is rigid in the ground state. The E,Zn-SOD1^{2SH} conformer, in turn, exchanges between monomeric and dimeric states with the former likely poised for binding the CCS (see above) so that the final steps in the maturation cycle can occur. Thus, the rare conformers that are sampled by intermediates along the pathway do provide an avenue by which the maturation process could occur. It is well established that there is selection pressure during evolution for a protein to adopt a particular native conformation required for function (43). In cases such as the maturation cycle of SOD1 or the DHFR enzyme cycle (42), it is of interest to ask whether evolution selects only for the final state or also for the process by which that state is formed, which would include, of course, the excited states along the pathway.

The melting temperatures of the SOD1 maturation states, related to their stabilities, have been tabulated in the literature: Cu,Zn-SOD1$^{S\text{-}S}$, 92 °C; E,Zn-SOD1$^{S\text{-}S}$, 75 °C; E,Zn-SOD1^{2SH}, 58 °C; apoSOD1$^{S\text{-}S}$, 59 °C; and apoSOD1^{2SH}, 48 °C (6, 11, 31). Interestingly, the number of excited-state conformations correlates inversely with stability, demonstrating the importance of posttranslational modifications in suppressing alternate conformations that might be important for cytotoxic interactions with cellular components. However, posttranslational modifications are not sufficient to rescue a disease phenotype. For example, our SEC assays (Fig. S5), focusing on the A4V disease mutant where the substitution of the smaller hydrophobic Ala side chain for Val considerably weakens the homodimer interface, shows that A4V apoSOD1^{2SH} is unable to bind CCS, unlike pWT apoSOD1^{2SH}. Zincation of the mutant only partially rescues binding, as A4V E,Zn-SOD1^{2SH} interacts with CCS less tightly than its pWT counterpart. Consequently, SOD1 may cause disease in some cases by overwhelming the cellular homeostatic machinery via the accumulation of less stable intermediates on the maturation pathway, as suggested by Morimoto and coworkers (44), rather than exclusively by formation of toxic conformers.

Materials and Methods

All of the variants of SOD1 were prepared in a pWT background where Cys-6 and Cys-111 have been replaced by Ala and Ser, respectively (45, 46); elimination of these surface residues avoids complications that could arise from intermolecular disulfide bond formation but maintains WT-like structure, folding, and enzymatic activity (1, 31, 47, 48). SOD1 proteins were overexpressed and purified as described previously (10) or using the following procedure: Cells were harvested and resuspended in 20 mM Hepes, pH 8, buffer containing 6 M GdnHCl and subsequently lysed by sonication. Following centrifugation to remove cellular debris (39,000 × *g* for 30 min at 4 °C), the supernatant was filtered and loaded onto a nickel column (GE Healthcare). After washing with 5 column-volumes of buffer (20 mM Hepes, pH 8, 6 M GdnHCl, 10 mM imidazole), SOD1 was refolded by washing with 10 column-volumes of a second buffer (20 mM Hepes, pH 8, 10 mM imidazole), after which the protein was eluted with buffer composed of 20 mM Hepes, pH 8, 400 mM imidazole. Dialysis of the eluate into TEV cleavage buffer (20 mM Tris, pH 8, 0.5 mM EDTA, 1 mM DTT) occurred overnight at 25 °C in the presence of TEV (1 mg TEV: 50 mg SOD1). Nickel chromatography was performed to isolate cleaved SOD1 in the flow-through, which was then concentrated and loaded onto an S75 size exclusion column and run with a buffer of 20 mM Hepes, pH 8. SOD1 was demetallated and reduced using standard protocols (31, 49). To produce E,Zn-SOD1 samples, $ZnCl_2$ was added to apoSOD1^{2SH} to achieve a stoichiometric ratio of 4 Zn:5 SOD1 (monomer) under dilute conditions (~60 μM or less) to avoid double zincation of SOD1 and subsequently concentrated. This mixture was left to incubate at room temperature for at least 30 min before measurements were taken and diagnostic HSQCs were collected at regular intervals to ensure that the sample did not change over time. ApoSOD1$^{S\text{-}S}$ was generated by diluting apoSOD1^{2SH} to ~10 μM in 20 mM Hepes, pH 8, after which 20 μM copper-1,10-phenantroline was introduced (50). The solution was stored at 37 °C for 3 h, and the reaction was subsequently quenched with 5 mM EDTA. A second round of gel filtration was employed to ensure no contamination with apoSOD1^{2SH}. Cu,Zn-SOD1$^{S\text{-}S}$ was generated as described previously (51).

ACKNOWLEDGMENTS. We thank Algirdas Velyvis for useful suggestions regarding DNA constructs. This work was supported by grants from the Canadian Institutes of Health Research and the Natural Sciences and Engineering Research Council of Canada. L.E.K. holds a Canada Research Chair in Biochemistry. R.M.C. was supported by grants from the Human Frontier Science Program (000793/2015-L) and the Canadian Institutes of Health Research (IRSC 0148000645).

1. Valentine JS, Doucette PA, Potter SZ (2005) Copper-zinc superoxide dismutase and amyotrophic lateral sclerosis. *Annu Rev Biochem* 74:563–593.
2. Robberecht W, Philips T (2013) The changing scene of amyotrophic lateral sclerosis. *Nat Rev Neurosci* 14:248–264.
3. Kato S, Saito M, Hirano A, Ohama E (1999) Recent advances in research on neuropathological aspects of familial amyotrophic lateral sclerosis with superoxide dismutase 1 gene mutations: Neuronal Lewy body-like hyaline inclusions and astrocytic hyaline inclusions. *Histol Histopathol* 14:973–989.
4. Gurney ME, et al. (1994) Motor neuron degeneration in mice that express a human Cu,Zn superoxide dismutase mutation. *Science* 264:1772–1775.
5. Karch CM, Prudencio M, Winkler DD, Hart PJ, Borchelt DR (2009) Role of mutant SOD1 disulfide oxidation and aggregation in the pathogenesis of familial ALS. *Proc Natl Acad Sci USA* 106:7774–7779.
6. Stathopulos PB, et al. (2006) Calorimetric analysis of thermodynamic stability and aggregation for apo and holo amyotrophic lateral sclerosis-associated Gly-93 mutants of superoxide dismutase. *J Biol Chem* 281:6184–6193.
7. Zetterström P, Graffmo KS, Andersen PM, Brännström T, Marklund SL (2013) Composition of soluble misfolded superoxide dismutase-1 in murine models of amyotrophic lateral sclerosis. *Neuromolecular Med* 15:147–158.
8. Zetterström P, et al. (2007) Soluble misfolded subfractions of mutant superoxide dismutase-1s are enriched in spinal cords throughout life in murine ALS models. *Proc Natl Acad Sci USA* 104:14157–14162.
9. Arnesano F, et al. (2004) The unusually stable quaternary structure of human Cu,Zn-superoxide dismutase 1 is controlled by both metal occupancy and disulfide status. *J Biol Chem* 279:47998–48003.
10. Sekhar A, et al. (2015) Thermal fluctuations of immature SOD1 lead to separate folding and misfolding pathways. *eLife* 4:e07296.
11. Furukawa Y, O'Halloran TV (2005) Amyotrophic lateral sclerosis mutations have the greatest destabilizing effect on the apo- and reduced form of SOD1, leading to unfolding and oxidative aggregation. *J Biol Chem* 280:17266–17274.
12. Banci L, et al. (2012) Human superoxide dismutase 1 (hSOD1) maturation through interaction with human copper chaperone for SOD1 (hCCS). *Proc Natl Acad Sci USA* 109:13555–13560.
13. Culotta VC, et al. (1997) The copper chaperone for superoxide dismutase. *J Biol Chem* 272:23469–23472.
14. Furukawa Y, Torres AS, O'Halloran TV (2004) Oxygen-induced maturation of SOD1: A key role for disulfide formation by the copper chaperone CCS. *EMBO J* 23:2872–2881.

15. Lamb AL, Torres AS, O'Halloran TV, Rosenzweig AC (2001) Heterodimeric structure of superoxide dismutase in complex with its metallochaperone. *Nat Struct Biol* 8: 751–755.
16. Rossi L, Marchese E, De Martino A, Rotilio G, Ciriolo MR (1997) Purification of a fully metal-depleted Cu, Zn superoxide dismutase from copper-deficient rat liver. *Biometals* 10:257–262.
17. Wang J, et al. (2002) Fibrillar inclusions and motor neuron degeneration in transgenic mice expressing superoxide dismutase 1 with a disrupted copper-binding site. *Neurobiol Dis* 10:128–138.
18. Steinkühler C, et al. (1991) Increase of Cu,Zn-superoxide dismutase activity during differentiation of human K562 cells involves activation by copper of a constantly expressed copper-deficient protein. *J Biol Chem* 266:24580–24587.
19. Sekhar A, Kay LE (2013) NMR paves the way for atomic level descriptions of sparsely populated, transiently formed biomolecular conformers. *Proc Natl Acad Sci USA* 110: 12867–12874.
20. Anthis NJ, Clore GM (2015) Visualizing transient dark states by NMR spectroscopy. *Q Rev Biophys* 48:35–116.
21. Sekhar A, et al. (2016) Probing the free energy landscapes of ALS disease mutants of SOD1 by NMR spectroscopy. *Proc Natl Acad Sci USA* 113:E6939–E6945.
22. Vallurupalli P, Sekhar A, Yuwen T, Kay LE (2017) Probing conformational dynamics in biomolecules via chemical exchange saturation transfer: A primer. *J Biomol NMR* 67: 243–271.
23. Palmer AG, 3rd, Kroenke CD, Loria JP (2001) Nuclear magnetic resonance methods for quantifying microsecond-to-millisecond motions in biological macromolecules. *Methods Enzymol* 339:204–238.
24. Mulder FAA, Skrynnikov NR, Hon B, Dahlquist FW, Kay LE (2001) Measurement of slow (microsecond-millisecond) time scale dynamics in protein side chains by N-15 relaxation dispersion NMR spectroscopy: Application to Asn and Gln residues in a cavity mutant of T4 lysozyme. *J Am Chem Soc* 123:967–975.
25. Leal SS, Cristóvão JS, Biesemeier A, Cardoso I, Gomes CM (2015) Aberrant zinc binding to immature conformers of metal-free copper-zinc superoxide dismutase triggers amorphous aggregation. *Metallomics* 7:333–346.
26. Strange RW, et al. (2003) The structure of holo and metal-deficient wild-type human Cu, Zn superoxide dismutase and its relevance to familial amyotrophic lateral sclerosis. *J Mol Biol* 328:877–891.
27. Crow JP, Sampson JB, Zhuang Y, Thompson JA, Beckman JS (1997) Decreased zinc affinity of amyotrophic lateral sclerosis-associated superoxide dismutase mutants leads to enhanced catalysis of tyrosine nitration by peroxynitrite. *J Neurochem* 69: 1936–1944.
28. Cao X, et al. (2008) Structures of the G85R variant of SOD1 in familial amyotrophic lateral sclerosis. *J Biol Chem* 283:16169–16177.
29. Broom HR, Rumfeldt JAO, Vassall KA, Meiering EM (2015) Destabilization of the dimer interface is a common consequence of diverse ALS-associated mutations in metal free SOD1. *Protein Sci* 24:2081–2089.
30. Wilcox KC, et al. (2009) Modifications of superoxide dismutase (SOD1) in human erythrocytes: A possible role in amyotrophic lateral sclerosis. *J Biol Chem* 284: 13940–13947.
31. Vassall KA, et al. (2011) Decreased stability and increased formation of soluble aggregates by immature superoxide dismutase do not account for disease severity in ALS. *Proc Natl Acad Sci USA* 108:2210–2215.
32. Ikura M, Kay LE, Bax A (1990) A novel approach for sequential assignment of ^{1}H, ^{13}C, and ^{15}N spectra of larger proteins: Heteronuclear triple-resonance three-dimensional NMR spectroscopy. Application to calmodulin. *Biochemistry* 29:4659–4667.
33. Wright GSA, Antonyuk SV, Hasnain SS (2016) A faulty interaction between SOD1 and hCCS in neurodegenerative disease. *Sci Rep* 6:27691.
34. Rodriguez JA, et al. (2002) Familial amyotrophic lateral sclerosis-associated mutations decrease the thermal stability of distinctly metallated species of human copper/zinc superoxide dismutase. *J Biol Chem* 277:15932–15937.
35. Kay LE, Torchia DA, Bax A (1989) Backbone dynamics of proteins as studied by ^{15}N inverse detected heteronuclear NMR spectroscopy: Application to staphylococcal nuclease. *Biochemistry* 28:8972–8979.
36. Henzler-Wildman KA, et al. (2007) A hierarchy of timescales in protein dynamics is linked to enzyme catalysis. *Nature* 450:913–916.
37. Papaleo E, et al. (2016) The role of protein loops and linkers in conformational dynamics and allostery. *Chem Rev* 116:6391–6423.
38. Waldauer SA, Bakajin O, Lapidus LJ (2010) Extremely slow intramolecular diffusion in unfolded protein L. *Proc Natl Acad Sci USA* 107:13713–13717.
39. Soranno A, et al. (2012) Quantifying internal friction in unfolded and intrinsically disordered proteins with single-molecule spectroscopy. *Proc Natl Acad Sci USA* 109: 17800–17806.
40. Rakhit R, et al. (2004) Monomeric Cu,Zn-superoxide dismutase is a common misfolding intermediate in the oxidation models of sporadic and familial amyotrophic lateral sclerosis. *J Biol Chem* 279:15499–15504.
41. Kayatekin C, Zitzewitz JA, Matthews CR (2008) Zinc binding modulates the entire folding free energy surface of human Cu,Zn superoxide dismutase. *J Mol Biol* 384: 540–555.
42. Boehr DD, McElheny D, Dyson HJ, Wright PE (2006) The dynamic energy landscape of dihydrofolate reductase catalysis. *Science* 313:1638–1642.
43. Hartl DL, Dykhuizen DE, Dean AM (1985) Limits of adaptation: The evolution of selective neutrality. *Genetics* 111:655–674.
44. Yu A, et al. (2014) Protein aggregation can inhibit clathrin-mediated endocytosis by chaperone competition. *Proc Natl Acad Sci USA* 111:E1481–E1490.
45. Broom HR, Rumfeldt JA, Meiering EM (2014) Many roads lead to Rome? Multiple modes of Cu,Zn superoxide dismutase destabilization, misfolding and aggregation in amyotrophic lateral sclerosis. *Essays Biochem* 56:149–165.
46. Lepock JR, Frey HE, Hallewell RA (1990) Contribution of conformational stability and reversibility of unfolding to the increased thermostability of human and bovine superoxide dismutase mutated at free cysteines. *J Biol Chem* 265:21612–21618.
47. Parge HE, Hallewell RA, Tainer JA (1992) Atomic structures of wild-type and thermostable mutant recombinant human Cu,Zn superoxide dismutase. *Proc Natl Acad Sci USA* 89:6109–6113.
48. McRee DE, et al. (1990) Changes in crystallographic structure and thermostability of a Cu,Zn superoxide dismutase mutant resulting from the removal of a buried cysteine. *J Biol Chem* 265:14234–14241.
49. Vassall KA, Stathopulos PB, Rumfeldt JAO, Lepock JR, Meiering EM (2006) Equilibrium thermodynamic analysis of amyotrophic lateral sclerosis-associated mutant apo Cu,Zn superoxide dismutases. *Biochemistry* 45:7366–7379.
50. Barthelme D, Chen JZ, Grabenstatter J, Baker TA, Sauer RT (2014) Architecture and assembly of the archaeal Cdc48*20S proteasome. *Proc Natl Acad Sci USA* 111: E1687–E1694.
51. Stathopulos PB, et al. (2003) Cu/Zn superoxide dismutase mutants associated with amyotrophic lateral sclerosis show enhanced formation of aggregates in vitro. *Proc Natl Acad Sci USA* 100:7021–7026.
52. Vallurupalli P, Bouvignies G, Kay LE (2012) Studying "invisible" excited protein states in slow exchange with a major state conformation. *J Am Chem Soc* 134:8148–8161.
53. Vallurupalli P, Hansen DF, Stollar E, Meirovitch E, Kay LE (2007) Measurement of bond vector orientations in invisible excited states of proteins. *Proc Natl Acad Sci USA* 104: 18473–18477.
54. Korzhnev DM, et al. (2004) Low-populated folding intermediates of Fyn SH3 characterized by relaxation dispersion NMR. *Nature* 430:586–590.
55. Delaglio F, et al. (1995) NMRPipe: A multidimensional spectral processing system based on UNIX pipes. *J Biomol NMR* 6:277–293.
56. Goddard T, Kneller D (2006) *Sparky—NMR Assignment and Integration Software* (University of California, San Francisco).
57. Sattler M, Schleucher J, Griesinger C (1999) Heteronuclear multidimensional NMR experiments for the structure determination of proteins in solution employing pulsed field gradients. *Prog Nucl Magn Reson Spectrosc* 34:93–158.
58. Cavanagh J, Fairbrother WJ, Palmer AG, Skelton NJ (1995) *Protein NMR Spectroscopy: Principles and Practice* (Academic, New York).
59. Farrow NA, et al. (1994) Backbone dynamics of a free and phosphopeptide-complexed Src homology 2 domain studied by ^{15}N NMR relaxation. *Biochemistry* 33:5984–6003.
60. Korzhnev DM, Skrynnikov NR, Millet O, Torchia DA, Kay LE (2002) An NMR experiment for the accurate measurement of heteronuclear spin-lock relaxation rates. *J Am Chem Soc* 124:10743–10753.
61. Ferrage F, Reichel A, Battacharya S, Cowburn D, Ghose R (2010) On the measurement of ^{15}N-^{1}H nuclear Overhauser effects. 2. Effects of the saturation scheme and water signal suppression. *J Magn Reson* 207:294–303.